Characterization of two-dimensional ultra-small-angle X-ray scattering apparatus for application to rubber filled with spherical silica under elongation

Yuya Shinohara,[a]* Hiroyuki Kishimoto,[b] Katsuaki Inoue,[c] Yoshio Suzuki,[c] Akihisa Takeuchi,[c] Kentaro Uesugi,[c] Naoto Yagi,[c] Kiyoshige Muraoka,[b] Tetsuo Mizoguchi[b] and Yoshiyuki Amemiya[a]

[a]Department of Advanced Materials Science, Graduate School of Frontier Sciences, The University of Tokyo, Japan, [b]SRI Research and Development Ltd, Japan, and [c]JASRI, Japan. Correspondence e-mail: shinohara@x-ray.k.u-tokyo.ac.jp

Two-dimensional ultra-small-angle X-ray scattering (2D-USAXS) apparatus at SPring-8 has been characterized. 2D-USAXS is a promising tool to study the structural change of the hierachical aggregate structure of fillers such as carbon black and silica particles in rubber. The aggregate structure of fillers is key to understanding the reinforcement effects which fillers show in rubber. We have applied 2D-USAXS to rubber filled with spherical silica particles and proved it to be a powerful technique.

1. Introduction

Addition of a filler such as carbon black and silica particles to an elastomer shows a reinforcement effect, which causes hysteresis loss and increases modulus, tear strength, tensile strength, and wear resistance (Ferry, 1980). The reinforcement effect has been extensively investigated since 1904, when S. C. Mote discovered it for carbon black, and various models have been proposed in order to explain it (Witten *et al.*, 1993; Heinrich *et al.*, 2002), although the mechanism of the reinforcement has not been clarified. Understanding of the relationship between the structure and mechanical properties of filled rubber is greatly important for industries such as the tire industry, from the viewpoint of ecology and tire safety. The mechanical properties of filled rubber depend not only on the volume fraction ϕ of the filler and the type of filler but also on their structure and their distribution. The structure and dispersion of filler in rubber have often been investigated using transmission electron microscopy (TEM). From TEM observation, it is known that fillers dispersing in rubber form a hierarchical structure: primary particles form aggregates, and the aggregates form agglomerates. These hierarchical structures range between 1 nm and 10 μm. It is, however, very difficult to investigate how these structures change under deformation of rubber by TEM. In addition, it requires a thin specimen, which makes it difficult to study the three-dimensional structure. Recent development of three-dimensional TEM (3D-TEM) (Koster *et al.*, 2000) enables us to observe the three-dimensional image of samples in real space. The damage due to the electron beam is, however, a serious problem when 3D-TEM is performed on soft materials. Also, time-resolved measurement of 3D-TEM is not available. Therefore, there remain problems associated with 3D-TEM for the structural study of filled rubber.

Ultra-small-angle X-ray scattering (USAXS) is a promising tool for structural study on this size scale. The high penetrating power of X-rays makes it possible to study the three-dimensional bulk structure of an opaque sample, which cannot be investigated by light scattering. USAXS has already been performed for the study of filled rubber (Riekel *et al.*, 1999, 2000; Ehrburger-Dolle *et al.*, 2001),

because it offers information about the fractal or non-fractal nature of the structure on a large size scale (agglomerate and aggregate) (Freltoft *et al.*, 1986; Hasmy *et al.*, 1994; Hyeon-Lee *et al.*, 1998). Such information cannot be obtained by conventional small-angle X-ray scattering, though it provides information about the structure of aggregates on a small size scale such as the roughness of the filler surface (Sinha *et al.*, 1988; Wong & Bray, 1988; Hoinkis *et al.*, 2004). Previous USAXS studies are often limited to static structures and one-dimensional measurements because an angle-scanning method is used in conventional USAXS. The angle-scanning method using Bonse–Hart camera (Bonse & Hart, 1965, 1966) has an advantage in obtaining high angular resolution data over a wide angular range. However, it is not appropriate for the measurement of materials with anisotropic structure because it requires too much time to obtain a whole two-dimensional scattering pattern. Furthermore, time-resolved experiments with sub-second time resolution are impossible with the scanning method. Two-dimensional USAXS (2D-USAXS) overcomes these drawbacks and offers a new approach in materials science to obtain three-dimensional information on complex materials. The use of high-intensity X-rays from third-generation synchrotron radiation makes it possible to observe anisotropic structural changes in real time. The long sample-to-detector distance makes it possible to observe 2D-USAXS patterns with sufficient angular resolution. 2D-USAXS has been performed at BL20XU, SPring-8 (Yagi & Inoue, 2003). We have developed and characterized time-resolved 2D-USAXS and have applied it to the real-time observation of filler dispersion states in stretched rubber. By combining the 2D-USAXS results with two-dimensional small-angle X-ray scattering (2D-SAXS) results at another beamline, we have successfully measured the anisotropic change in the scattering pattern over a wide size scale range and have investigated the relationship between the viscoelastic properties and the structural changes in the filler network in rubber under stretching.

In the present article, we first report the characterization of 2D-USAXS at BL20XU, SPring-8. Then we show the application of 2D-USAXS to filled rubber. The quantitative analysis of rubber filled with carbon black and silica particles requires the use of unified

Table 1
Recipes of samples.

	SH100	SH300
SBR	100	100
Stearic acid	2	2
Silica (282.9 nm)		53.2
Silica (111.1 nm)	79.8	
Si 69†	10.83	7.22
Acc. NS‡	1	1
Acc. D§	1	1
Sulfur	1.5	1.5

† Silane coupling agent. ‡ *N-tert*-Butyl-2-benzothiazolesulfenamide. § 1,3-Diphenyl-guanidine.

functions (Beaucage & Schreafer, 1994; Beaucage 1995, 1996) and we have successfully applied time-resolved 2D-USAXS to such a complicated system. In this article, however, we show the application of 2D-USAXS to a model filler, spherical silica particles with a monodispersive size distribution, in stretched rubber.

2. Experimental setup

2.1. Materials

The recipes and cure conditions for preparation of the rubber samples are listed in Table 1. As model samples, styrene-butadiene rubber (SBR) filled with spherical silica particles (Seahoster, Nippon Shokubai) with an almost monodispersive size distribution was used. Two types of silica particles (SH300, average diameter = 282.9 nm, and SH100, average diameter = 111.1 nm) with different sizes were added. The size distribution of each sample was measured using TEM and SAXS for a diluted sample. The results showed that both samples have a Gaussian size distribution with variances of 6.37% (SH300) and 7.8% (SH100). Ingredients were mixed in an internal mixer until the temperature of the compound reached 423 K. The compound was vulcanized at 423 K for 35 min to form a sheet about 1 mm thick. In this process, silica particles and rubber polymers were covalently bonded *via* silane coupling agents. The volume fraction of filler was 20% for SH300 and 30% for SH100.

2.2. Two-dimensional USAXS and SAXS

2D-USAXS experiments were performed at the 'medium-length beamline' BL20XU, SPring-8 (Hyogo, Japan) (Suzuki *et al.*, 2004; Yagi & Inoue, 2003). A schematic view of the experimental setup is shown in Fig. 1. This beamline uses a planar in-vacuum undulator as
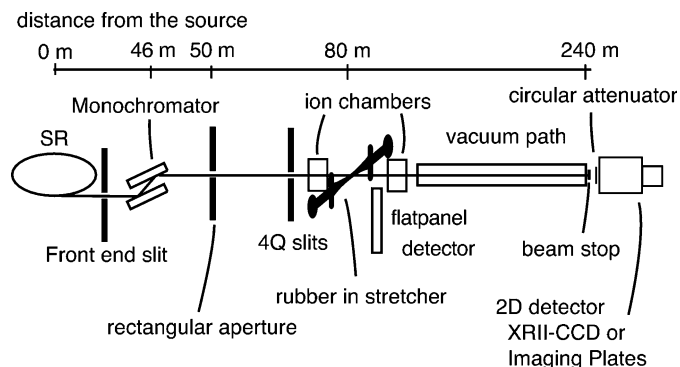

Figure 1
Schematic view of the experimental setting. The sample was placed in a uniaxial stretcher. The distance between the sample and the USAXS detector was 160.5 m. The two-dimensional detectors and the stretcher were remotely controlled.

an X-ray source (Hara *et al.*, 1998). The first hutch in the ring building is about 80 m from the source, and the second hutch in the Biomedical Imaging Center is at 240 m. The two hutches are connected by a vacuum pipe with an inner diameter of 10 cm. The windows of the pipe are made of Kapton films. Samples were placed at the first hutch and 2D-USAXS detectors were set at the second hutch. The sample-to-detector distance was 160.5 m and the X-ray energy was 23 keV. Three sets of slits were used to define the beam size and the SAXS resolution. One was a front-end slit (FE slit), which was placed upstream of the monochromator 46 m from the source. Another one was a rectangular aperture, which was set at the optical hutch in the ring building around 50 m from the source. Three sizes of aperture (20, 50 and 100 µm on a side) can be selected. The slit and the aperture limited the size and divergence of X-ray beam, which is described in the next section. A four-quadrant slit (4Q slit) that was placed just before the sample was used to remove parasitic scattering. The beam stop was 3 mm in diameter and was placed just behind the exit window of the vacuum pipe. In this setup, USAXS in a q range of 1.5×10^{-4}–2.5×10^{-3} Å^{-1} was recorded, where q is the magnitude of the scattering vector defined as $q = 4\pi\sin\theta/\lambda$, where λ is the X-ray wavelength and 2θ is the scattering angle. Two-dimensional X-ray detectors such as an imaging plate (IP) and a cooled charge-coupled device (CCD) detector (C4880-40-26A, Hamamatsu Photonics Ltd.) coupled with an X-ray image intensifier (V7339P, Hamamatsu Photonics Ltd., XRII) (Amemiya *et al.*, 1995) were used to record 2D-USAXS. The use of an XRII-CCD enables us to perform a real-time measurement with its high-sensitivity, while distortion-free images with wide dynamic range are available by the use of an IP. In order to overcome the narrow dynamic range of the XRII-CCD, we placed a circular attenuator of aluminium just before the detectors to attenuate the high scattering intensity at the center of the image if necessary. Further, we used only the center part of the XRII-CCD in order to avoid unnecessary image distortion and contrast distortion (Ito *et al.*, 2005). The transmittance of the sample was measured by two sets of ion chambers in real time. The change of molecular orientation of rubber under elongation was simultaneously measured by time-resolved wide-angle X-ray scattering (WAXS) using an X-ray flat-panel detector in order to investigate the relationship between the structural change of the filler aggregate and the orientation of the polymer. A direct beam was observed with a Beam Monitor 2 (Yagi *et al.*, 1999) coupled with a cooled CCD camera.

2D-SAXS experiments were performed at BL40B2, SPring-8. The X-ray energy used was 8 keV and the camera distance was around 3100 mm, which was calibrated by the first peak of silver behenate. An XRII-CCD, a two-dimensional position-sensitive proportional counter (RAPID) (Lewis *et al.*, 1997) and an IP were used to record 2D-SAXS patterns. In this setup, SAXS in a q range of 1.5×10^{-3}–0.1 Å^{-1} was recorded.

In each measurement, samples were placed on a uniaxial stretching machine, where the load and the sample strain were measured in real time. The initial length of the sample was 4 mm. The elongation ratio was 2 mm s^{-1} and the USAXS and SAXS images were recorded at intervals of 2 s (XRII-CCD) or 0.5 s (RAPID).

3. Results and discussion

3.1. Characterization of time-resolved 2D-USAXS

In order to perform time-resolved 2D-USAXS, we have improved three factors: the SAXS resolution, the intensity of the incident X-ray beam, and the smearing of scattering intensity profiles. The SAXS resolution is determined by the beam size and the beam divergence,

as well as by parasitic scattering. Small beam size and beam divergence allow us to use a small beamstop, although they often lead to insufficient intensity of the incident X-ray beam to perform time-resolved measurements. Fig. 2 (left) shows the image of the direct X-ray beam at the USAXS detector position taken by the beam monitor. It is clearly seen that the beam is large and elliptic when no aperture is installed, while use of the small rectangular aperture leads to an isotropic beam. It should be noted that the image shows a Fraunhofer diffraction pattern from a rectangular aperture when we use the rectangular apertures with sides of 20 and 50 µm. The diffraction pattern was successfully eliminated by the 4Q slits just before the sample, and it had no effect on USAXS data quality. The apertures with sides of 20 and 50 µm both show isotropic beam profiles, while the size becomes larger due to diffraction when we use the aperture of 20 µm. Therefore, we used the aperture of 50 µm. In this case, the size of the beam was 100 µm (full width at half-maximum, FWHM) and 340 µm (full-width at 1% of maximum) at the sample position, and 380 µm (FWHM) and 1.6 mm (full-width at 1% of maximum) at the USAXS detector position. In our experiments, we used a beamstop with a diameter of 3 mm in order to prevent the direct X-ray beam from impinging on the detector, because the X-rays sometimes change their position due to the fluctuation of the monochromator as described below. In this case, the minimum of q was 1.5×10^{-4} Å^{-1}. Fig. 2 (right) shows the dependence of the X-ray intensity at the sample position on the FE slit size and the size of the rectangular aperture. When we used the 50 µm aperture, the intensity with FE slits of 120 µm × 90 µm was ten times larger than that with FE slits of 30 µm × 30 µm. In Fig. 3 (left), smearing effects are compared between the above two cases. Fig. 3 (left) shows normalized one-dimensional USAXS intensity profiles of SBR filled with another type of Seahoster particles (average diameter 1500 nm, volume fraction 20%), which are obtained by azimuthally averaging 2D-USAXS data. The data show no difference in smearing between the data with the smallest FE slit size and the largest FE slit size.

Although time-resolved 2D-USAXS is now routinely performed for structural analysis of filled rubber using the above conditions, there remain some problems to be solved. (1) Stability of the X-ray beam position. Because the distance between the monochromator and the detector is around 200 m, a small fluctuation of the monochromator causes a significant change of the beam position at the detector. If the angle of th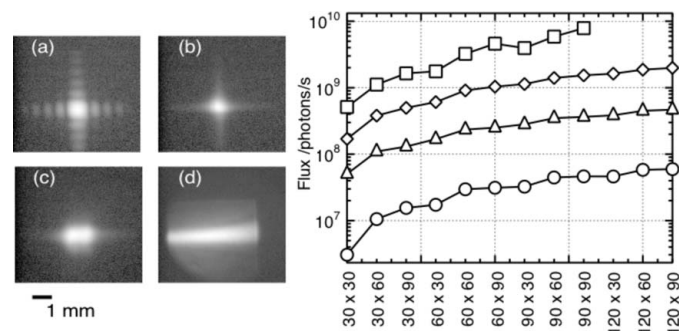e monochromator changes by $7.5 \times$ 10^{-3} mrad, the whole of the direct beam impinges on the detector, which would destroy the XRII. This is an extreme case. However, a small change of the monochromator angle leads to an unstable beam centre position. This sometimes makes the analysis procedure complicated. (2) Appearance of a speckle pattern. Because we use a small aperture, the beam size at the sample position is comparable with the transverse coherence length, which is roughly estimated to be 30 µm assuming the rectangular aperture is an imaginary light source. Also, the longitudinal coherence length easily satisfies the condition of speckle observation, because we measure ultra-small-angle scattering. Therefore, what we measure is the speckle pattern. Though it indicates the availability of X-ray photon correlation spectroscopy measurement (XPCS) in this ultra-small-angle region, XPCS measurement at this beamline is difficult at present and the speckle is simply the origin of noisy USAXS data. This is because the beam moves on the sample rapidly due to the fluctuation of the monochromator, and the observed speckle pattern changes rapidly. It prevents us from obtaining significant XPCS data and no meaningful datum is obtained at present. (3) Narrow range of scattering angle. The beamline was originally designed not for scattering, but for medical applications such as imaging. Therefore, the diameter of the vacuum pipe connecting the first and second hutches is not very large, 10 cm. This limits the maximum of q to 2.5×10^{-3} Å^{-1}, and makes it difficult to measure scattering patterns over a wide q range. In order to overcome this drawback, we combined USAXS results obtained at BL20XU with SAXS results obtained at BL40B2. Fig. 3 (right) shows typical one-dimensional USAXS–SAXS intensity profiles, which were obtained by azimuthally averaging two-dimensional data. At BL40B2, SAXS in a q range of 1.5×10^{-3}–0.1 Å^{-1} was recorded. Therefore, by combining the USAXS and SAXS, we obtained structural information in the range of nm to µm.

3.2. Structural change of rubber filled with spherical silica

In this section, the application of 2D-USAXS to filled rubber is described. We used spherical silica particles with a well defined size distribution as filler. Note that such a system with smaller particles has already been investigated experimentally and with computer simulation (Rharbi *et al.*, 1999; Oberdisse *et al.*, 2000; El Harrak *et al.*, 2006) and that similar scattering patterns to those described below
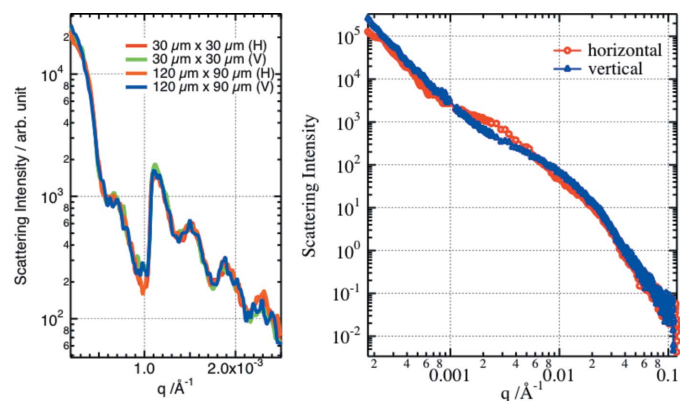

Figure 2
(Left) Image of X-ray beam at the USAXS detector position on a log scale. The front-end slit size was 30 µm × 30 µm. The rectangular aperture size was (*a*) 20 µm, (*b*) 50 µm, (*c*) 100 µm. (*d*) Image without a rectangular aperture. (Right) Dependence of the intensity of the incident X-ray beam on the size of the front-end slit and that of the rectangular aperture. The size of the front-end slit (horizontal/µm × vertical/µm) is taken in the abscissa. The size of the rectangular aperture was 20 µm (circles), 50 µm (triangles), and 100 µm (diamonds). Squares show the results without a rectangular aperture.

Figure 3
(Left) Normalized one-dimensional USAXS intensity profiles. The scattering intensity is normalized by the incident X-ray intensity measured by the ion chamber. The scattering intensity of $q < 1.05 \times 10^{-3}$ Å^{-1} was attenuated by the circular attenuator of aluminium (4 mm thick) which was placed just before the detector. The size of the rectangular aperture was 50 µm. (Right) Typical USAXS–SAXS intensity profiles of filled rubber under elongation. The horizontal direction is the elongation direction. The profiles are obtained by azimuthally averaging two-dimensional data.

were obtained. Fig. 4 shows the stress–strain curve and corresponding USAXS images. The images show corresponding hysteresis to that of the stress–strain curve. Therefore, the morphology of the aggregation is clearly found to affect the hysteresis of the stress–strain curve. This is the first time, to our knowledge, that the hysteresis of an aggregate structure during the loading and unloading process has been observed. There are mainly two kinds of information in these images. At a low q region, an upturn is observed, which would suggest the existence of aggregates. However, we do not discuss it here, because the q range is not low enough to evaluate the size and form of the aggregates. Future work using 8 keV X-rays instead of 23 keV X-rays is expected to give information on this matter. On the other hand, a double-wing or a four-point pattern is observed at a higher q region. These patterns would correspond to the correlation between primary particles forming the aggregates. The origins of this double-wing and the four-point pattern have already been discussed (Rharbi *et al.*, 1999). However, there is a decisive difference between our sample and the materials used in the previous papers. In our case, silica particles and rubber polymers are covalently bonded *via* silane coupling agents, while there is no chemical bonding between silica particles and polymers in the previous work. Therefore, the origin of these characteristic patterns should be carefully discussed from the different aspect. Detailed discussion will appear elsewhere. In this manuscript, we only show the analysis along the stretching direction. In this case, structure factor is usually more appropriate to show the aggregation structure than scattering intensity. The form factor, $F(q)$, of the spherical silica can be calculated using the scattering function of a spherical particle,

$$F(q) = (\Delta\rho V)^2 \frac{[3\sin(qR) - qR\cos(qR)]^2}{(qR)^6}$$

where R is the radius of the sphere, $\Delta\rho$ is the contrast of electron density, and V is the volume of the sphere. By dividing $I(q)$ by $F(q)$ and considering the size distribution of the particles, we calculated the structure factor, $S(q)$. Fig. 5 shows the change of the structure factor along the stretching direction during the loading process, where ε is the elongation ratio defined by $\Delta L/L$, L is the initial length, and ΔL is the elongation length of a sample. At first, a peak at $q = 2.00 \times 10^{-3}$ Å^{-1} is observed, which corresponds to the distance between neighboring silica particles. This value is different from the

Figure 5
Profiles of one-dimensional structure factor of SH300 along the stretching direction. The profiles are shifted vertically for clarity. Before elongation, a peak at $q = 2 \times 10^{-3}$ Å^{-1} is observed. On stretching the samples, the peak moves to a lower angle, and an additional peak appears at around 2.05×10^{-3} Å^{-1}.

case when neighboring particles make contact with each other (in this case, $q = 2.2 \times 10^{-3}$ Å^{-1}), thus suggesting that there are polymer chains between neighboring particles and that the particles form aggregates without close packing. When we stretch the sample, the peak moves to a lower angle (7.95×10^{-4} Å^{-1} at $\varepsilon = 2.5$), which describes how the distance between neighboring silica particles increases along the stretching direction. The distance increases proportionally when the strain increases. At high strain, an additional peak appears at $q = 2.05 \times 10^{-3}$ Å^{-1}, and the position of this additional peak does not change. This additional peak corresponds to the distance between spherical silica particles connected *via* rubber polymers. It is noted that this appearance corresponds to the increase of the elastic modulus, which indicates that the polymer chains between the silica cannot be stretched any more and that it shows high entropic elasticity. This highly stretched rubber would be one of the origins of the reinforcement. However, analysis of the precise mechanism requires information about the states of rubber near the silica particles and will be discussed elsewhere.
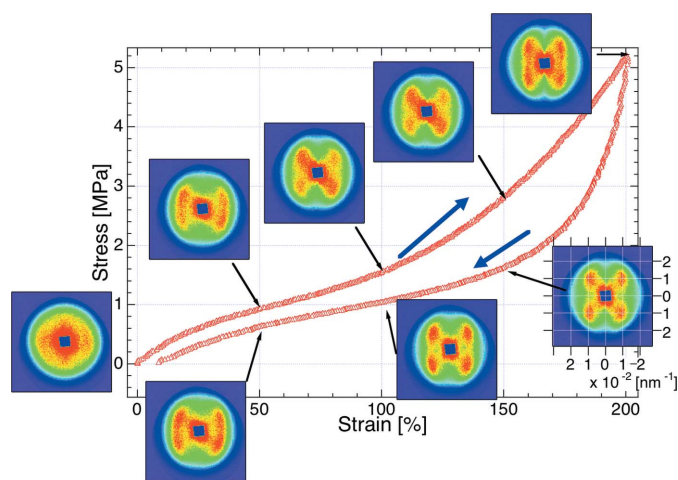

Figure 4
Stress–strain curve of SH300 and corresponding 2D-USAXS images during the loading and unloading process. The sample is stretched in the horizontal direction. The scale of the scattering vector is shown in one of the images.
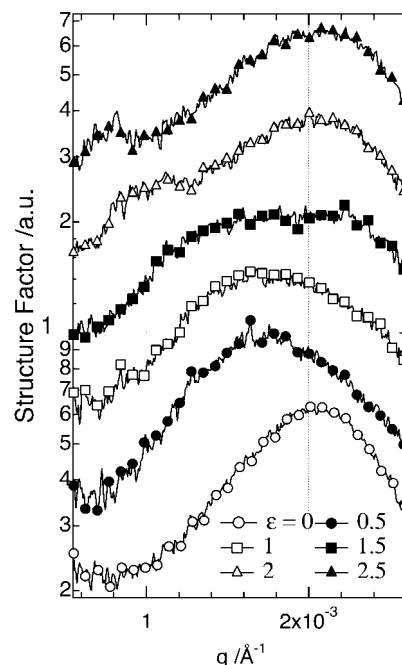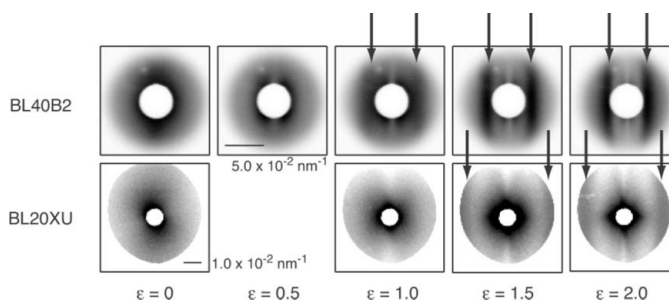

Figure 6
2D-USAXS and 2D-SAXS images of SH100 during the loading process. Black arrows show the peak corresponding to the distance between neighboring silica particles, which starts to appear under high strain. The USAXS image at $\varepsilon = 0.5$ was not measured.

Next we show the result for SH100. Fig. 6 shows 2D-USAXS images at BL20XU and 2D-SAXS images at BL40B2 of SH100 during the loading process. In this case, $S(q)$ can be approximated by $I(q)$. For the data at BL20XU, q is sufficiently small and the use of $I(q)$ instead of $S(q)$ has no problems. For the data at BL40B2, q is not sufficiently small and the pattern of $I(q)$ is not exactly the same as that of $S(q)$, but is confirmed to be similar to the real $S(q)$, which is very noisy. Therefore, we show only the images of $I(q)$ instead of $S(q)$. Before elongation, both USAXS and SAXS show anisotropy, which would arise in the sample preparation process. By increasing the elongation ratio, USAXS images at BL20XU show a butterfly pattern, which is well known for a stretched gel (Bastide & Leibler, 1988). In the case of a stretched gel, the butterfly pattern originates from the inhomogeneity of cross-links under elongation. In our case, the pattern would be caused by the inhomogeneous distribution of silica aggregates. It should be noted that additional peaks, as shown by black arrows, appear when $\varepsilon > 1.0$. The peaks correspond to the distance between neighboring silica particles. The distance between neighboring silica particles is plotted in Fig. 7 (left). At $\varepsilon = 0.75$, the peaks appear and then the distance between silica particles increases with increasing strain. These results suggest that the rubber between silica aggregates should be stretched first and then the rubber between neighboring silica particles should be highly stretched. Fig. 7 (right) shows stress–strain curves and anisotropy ratios that were calculated from the WAXS images. Here the anisotropy ratio, AR, is defined simply as $AR = I_1/I_2$, where I_1 is the scattering intensity perpendicular to the elongation and I_2 is that parallel to the elongation. The results for rubber without filler are also shown for comparison. The increase of elastic modulus and the anisotropy ratio correspond well to the appearance of the additional peak in USAXS–SAXS at around $\varepsilon = 0.75$. This result supports the above idea that the highly stretched polymer connecting silica particles is one of the origins of the high elastic modulus under large strain. Note that the anisotropic ratio and the elastic modulus keep small values and the additional peaks do not appear in the case of silica-filled rubber without silane coupling agent, which covalently connects the silica particle and rubber (Shinohara et al., 2007). This also supports the above deformation model.

4. Summary

We characterized 2D-USAXS at SPring-8 and determined the optimal conditions for 2D-USAXS. By using two-dimensional USAXS–SAXS, the structural change of filled rubber was observed. It revealed the relationship between the deformation of aggregate structure, polymer orientation, and mechanical properties of rubber filled with spherical silica particles. Further quantitative study using two-dimensional USAXS–SAXS will elucidate the age-old unsolved mechanism of the reinforcement in filled rubber.

References

Amemiya, Y., Ito, K., Yagi, N., Asano, Y., Wakabayashi, K., Ueki, T. & Endo, T. (1995). *Rev. Sci. Instrum.* **66**, 2290–2294.
Bastide, J. & Leibler, L. (1988). *Macromolecules*, **21**, 2647–2649.
Beaucage, G. (1995). *J. Appl. Cryst.* **28**, 717–728.
Beaucage, G. (1996). *J. Appl. Cryst.* **29**, 134–146.
Beaucage, G. & Schreafer, D. (1994). *J. Non-Cryst. Solids*, **172–174**, 797–805.
Bonse, U. & Hart, M. (1965). *Appl. Phys. Lett.* **7**, 238–240.
Bonse, U. & Hart, M. (1966). *Z. Phys.* **189**, 151–162.
Ehrburger-Dolle, M., Hinderman-Bischoff, M., Livet, F., Brey, F., Rochas, C. & Geissler, E. (2001). *Langmuir*, **17**, 329–334.
El Harrak, A., Carrot, G., Jestin, J., Oberdisse, J. & Boué, F. (2006). *XIIIth International Conference on Small-Angle Scattering*, Abstracts, p. 217.
Ferry, J. D. (1980). *Viscoelastic Properties of Polymers*. New York: John Wiley and Sons.
Freltoft, T., Kjems, J. & Sinha, S. (1986). *Phys. Rev. B*, **33**, 269–275.
Hara, T., Tanaka, T., Tanabe, T., Maréchal, X.-M., Okada, S. & Kitamura, H. (1998). *J. Synchrotron Rad.* **5**, 403–405.
Hasmy, A., Vacher, R. & Jullien, R. (1994). *Phys. Rev. B*, **50**, 1305–1308.
Heinrich, G., Kluppel, M. & Vilgis, T.A. (2002). *Curr. Opin. Solid State Mater. Sci.* **6**, 195–203.
Hoinkis, E., Lima, E. & Schuvert-Bischoff, O. (2004). *Langmuir*, **20**, 8823–8830.
Hyeon-Lee, J., Beaucage, G., Pratsinis, S. & Vemury, S. (1998). *Langmuir*, **14**, 5751–5756.
Ito, K., Kamikubo, H., Yagi, N. & Amemiya, Y. (2005). *Jpn. J. Appl. Phys.* **44**, 8684–8691.
Koster, A., Ziese, U., Verkleij, A., Janssen, A. & de Jong, K. (2000). *J. Phys. Chem. B*, **104**, 9368–9370.
Lewis, R., Helsby, W., Jones, A., Hall, C., Parker, B., Sheldon, J., Clifford, P., Hillen, M., Summer, I., Fore, N., Jones, R. & Roberts, K. (1997). *Nucl. Instrum. Methods A*, **392**, 32–41.
Oberdisse, J., Rharbi, Y. & Boué, F. (2000). *Comput. Theor. Polym. Sci.* **10**, 207–217.
Rharbi, Y., Cabane, B., Vacher, A., Joanicot, M. & Boué, F. (1999). *Europhys. Lett.* **46**, 472–478.
Riekel, T., Hindermann-Bischoff, M. & Ehrburger-Dolle, F. (2000). *Langmuir*, **16**, 5588–5592.
Riekel, T., Misono, S. & Ehrburger-Dolle, F. (1999). *Langmuir*, **15**, 914–917.
Shinohara Y., Kishimoto H. & Amemiya Y. (2007). In preparation.
Sinha, S., Sirota, E., Garoff, S. & Stanley, H. (1988). *Phys. Rev. B*, **38**, 2297–2311.
Suzuki, Y., Uesugi, K., Takimoto, N., Fukui, T., Aoyama, K., Takeuchi, A., Takano, H., Yagi, N., Mochizuki, T., Goto, S., Takeshita, K., Takahashi, S., Ohashi, H., Furukawa, Y., Ohata, T., Matushita, T., Ishizawa, Y., Yamazaki, H., Yabashi, M., Tanaka, T., Kitamura, H. & Ishikawa, T. (2004). *Am. Inst. Phys. Proc.* **705**, 344–347.
Witten, T., Rubinstein, M. & Colby, R. (1993). *J. Phys. (Paris)*, **3**, 367–383.
Wong, P-J. & Bray, A. (1988). *J. Appl. Cryst.* **21**, 786–794.
Yagi, N., Endo, T., Suzuki Y. & Kohmura, Y. (1999). *SPring-8 Annual Report 1998*, p. 177.
Yagi, N. & Inoue, K. (2003). *J. Appl. Cryst.* **36**, 783–786.
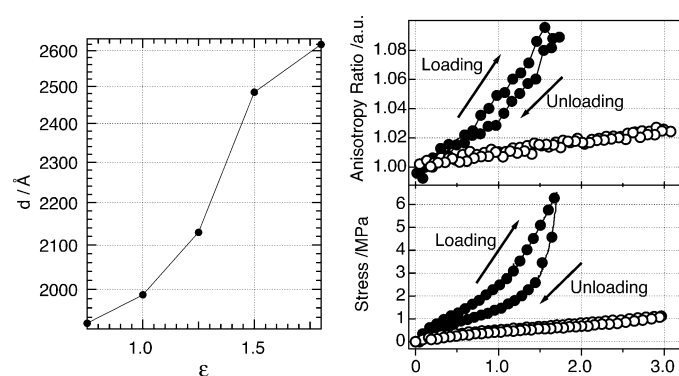
Figure 7
(Left) Distance between neighboring silica particles in real space. At $\varepsilon < 0.75$, the peak is invisible. (Upper right) Anisotropy ratio during the loading and unloading process of SH300. (Lower right) Stress–strain curve of SH300 during the loading and unloading process. In both figures, filled circles show the result of SH100, while open circles show that of unfilled rubber. Around $\varepsilon = 0.75$, the anisotropy ratio and the stress of SH100 increase.